Analysis of test beam data taken with a prototype of TPC with resistive Micromegas readout for the T2K Near Detector upgrade

D. Attié[a], O. Ballester[h], M. Batkiewicz-Kwasniak[b], P. Billoir[c], A. Blanchet[c], A. Blondel[c], S. Bolognesi[a], R. Boullon[a], D. Calvet[a], M. P. Casado[h,m], M.G. Catanesi[d], M. Cicerchia[e], G. Cogo[f], P. Colas[a], G. Collazuol[f], C. Dalmazzone[c], T. Daret[a], A. Delbart[a], A. De Lorenzis[h,l], K. Dygnarowicz[i], J. Dumarchez[c], S. Emery-Schrenk[a], A. Ershova[a], G. Eurin[a], M. Feltre[f], C. Forza[f], L. Giannessi[f], C. Giganti[c], F. Gramegna[e], M. Grassi[f], M. Guigue[c], P. Hamacher-Baumann[g], S. Hassani[a], D. Henaff[a], F. Iacob[f], C. Jesús-Valls[h], S. Joshi[a], R. Kurjata[i], M. Lamoureux[f], A. Langella[k], J. F. Laporte[a], L. Lavitola[k], M. Lehuraux[a], A. Longhin[f], T. Lux[h], L. Magaletti[d], T. Marchi[e], A. Maurel[a], L. Mellet[c], M. Mezzetto[f], L. Munteanu[a], Q. V. Nguyen[c], Y. Orain[c], M. Pari[f], J.-M. Parraud[c], C. Pastore[d], A. Pepato[f], E. Pierre[c], C. Pio Garcia[h], B. Popov[c], H. Przybiliski[b], F. Pupilli[f], T. Radermacher[g], E. Radicioni[d], M. Riallot[a], S. Roth[g], S. Russo[c], A. Rychter[i], L. Scomparin[f], D. Smyczek[g], J. Steinmann[g], S. Suvorov[c,j], J. Swierblewski[b], D. Terront[c], N. Thamm[g], F. Toussenel[c], V. Valentino[d], M. Varghese[h], G. Vasseur[a], U. Virginet[c], U. Yevarouskaya[c,1], M. Ziembicki[i], M. Zito[c]

[a] *IRFU, CEA, Université Paris-Saclay, Gif-sur-Yvette, France*
[b] *H. Niewodniczanski Institute of Nuclear Physics PAN, Cracow, Poland*
[c] *LPNHE, Sorbonne Université, Université de Paris, CNRS/IN2P3, Paris; France*
[d] *INFN sezione di Bari, Università di Bari e Politecnico di Bari, Italy*
[e] *INFN: Laboratori Nazionali di Legnaro (LNL), Padova , Italy*
[f] *INFN Sezione di Padova and Università di Padova, Dipartimento di Fisica e Astronomia, Padova, Italy*
[g] *RWTH Aachen University, III. Physikalisches Institut, Aachen, Germany*
[h] *Institut de Física d'Altes Energies (IFAE) - The Barcelona Institute of Science and Technology (BIST), Campus UAB, 08193 Bellaterra (Barcelona), Spain*
[i] *Warsaw University of technology, Warsaw, Poland*
[j] *Institute for Nuclear Research of the Russian Academy of Sciences, Moscow, Russia*
[k] *INFN Sezione di Napoli and Università di Napoli Federico II, Dipartimento di Fisica, Napoli, Italy*

*Corresponding author
[1] uyevarou@lpnhe.in2p3.fr

[l]Qilimanjaro Quantum Tech, Barcelona 08007, Spain
[m]Departament de Física, Universitat Autònoma de Barcelona

Abstract

In this paper we describe the performances of a prototype of the High Angle Time Projection Chambers (HA-TPCs) that are being produced for the Near Detector (ND280) upgrade of T2K. The two HA-TPCs of ND280 will be instrumented with eight Resistive MicroMegas modules (ERAM) on each endplate. This innovative techniques allows to detect the charge emitted by ionization electrons over several pads, improving the determination of the track position.

The TPC prototype has been equipped with the first ERAM module produced for T2K and with the HA-TPC electronics chain and it has been exposed to the DESY Test Beam in order to measure spatial and dE/dx resolution. In this paper we characterize the performances of the ERAM and, for the first time, we compare them with a newly developed simulation of the detector.

Spatial resolution better than 800 μm and dE/dx resolution better than 10% are observed for all the incident angles and for all the drift distances of interest. All the main features of the data are correctly reproduced by the simulation and these performances fully fulfill the requirements for the HA-TPCs of T2K.

Keywords: Resistive Micromegas, T2K Near Detector Time Projection Chambers

Contents

1. Introduction

T2K is a long-baseline neutrino oscillation experiment that is taking data in Japan since 2010 [1]. By using an intense muon neutrino beam produced at the J-PARC accelerator complex and searching for the appearance of electron neutrinos at the far detector, Super-Kamiokande, T2K provided the first indications of θ_{13} mixing angle being different from zero [1] followed by the first measurement of neutrino oscillations in appearance mode [2]. Recently first hints of Charge-Parity (CP) violation in the leptonic sector were also published by T2K [3].

In order to confirm these hints, T2K is now preparing the second phase of the experiment, that includes an upgrade of the neutrino beamline [4] and of the off-axis Near Detector complex, ND280 [5].

ND280 is a magnetized multi-purpose detector with several sub-detectors installed inside the UA1 magnet that provide a magnetic field of 0.2 T. The core of ND280 is a tracker system, composed by two Fine Grained Detectors (FGDs) [6] and three Time Projection Chambers (TPCs) [7] instrumented with Bulk Micromegas modules [8]. The TPCs are used to track charged particles emitted in neutrino interactions and measure their charge and momentum and perform particle identification based on the ionization in the gas. ND280 has been extensively used in all T2K oscillation analyses and allows to reduce systematic uncertainties to the 4–5% level [9].

An upgrade of ND280 is being constructed[10], with the goal of further reducing these uncertainties [11]. It consists in replacing one of the ND280 sub-detectors, the P0D, with a new tracker system composed by a 3-dimensional scintillator target (Super-FGD) [12], made of $\sim$2 millions of 1 cm^3 scintillator cubes each readout by three wavelength shifting fibers, two High Angle TPCs (HA-TPCs) and six Time-Of-Flight (TOF) planes [13]. Among other improvements, this upgrade, that will be installed in J-PARC in 2023, is expected to have better efficiency to reconstruct high angle and backward going tracks emitted in neutrino or antineutrino interactions thanks to the presence of the HA-TPCs.

Each endplate of the HA-TPC will be instrumented with 8 Encapsulated Resistive Anode Micromegas (ERAM). This technology, initially developed for the ILC prototypes [14], allows to detect the charge induced by ionization electron on one pad over several pads ('spread'), improving the spatial resolution and hence the determination of the momentum of the charge particles. Different ERAM prototypes have been tested at CERN [15] and at

DESY [16] to characterize the ERAM response for horizontal tracks and for inclined tracks at short drift distances. The results of these test beams allowed to validate the ERAM design and start the production of the 32 ERAMs that will be used to instrument the HA-TPCs.

The first of these ERAM detectors was tested using an X-ray test bench at CERN and then mounted in a prototype of the field cages that are being constructed for the HA-TPCs. This field cage prototype has the same construction materials (discussed in Sec.2.1), the same drift length ($\sim$ 1 m) and the same strip foils configuration to produce a uniform electric field as the cages that are being constructed for the ND280 Upgrade. Also the front-end electronics chain that will be used for the HA-TPCs, including two Front-End-Cards (FEC) each hosting eight AFTER chips [17], and one Front-End-Mezzanine (FEM) both equipped with their cooling plates was mounted on the field cage. The FEM was connected to Trigger and Data Concentrator Module (TDCM) electronic readout [18].

The TPC was placed at the DESY T24/1 facility [19] inside a large-bore superconducting solenoid, called PCMAG, that provides a magnetic field of up to 1.25 T and it was exposed to an electron beam with momenta between 1 and 4 GeV/c. As we will show in this paper, this test beam campaign allowed to validate the performances of the TPCs for tracks with different incident angles with respect to the ERAM detector and for all the drift distances of interest for the T2K TPCs. With respect to the results presented in [16], the ERAM performances are compared with a simulation that has been developed by using the ND280 software, adding the HA-TPCs ERAM geometry and the features of the resistive layers and of the AFTER electronics response.

As we will show in the rest of this paper, the ERAM detector allows to reach an excellent spatial resolution, below 800 μm for all the incident angles and drift distances, and an excellent dE/dx resolution, below 10% for tracks crossing the entire ERAM module. These performances are in good agreement with the ones predicted by the simulation that is able to reproduce both, low level variables, such as the charge sharing between neighboring pads or their time difference, as well as the spatial and the dE/dx resolution.

2. Experimental setup

2.1. HA-TPC field cage prototype

One of the main innovations of the HA-TPCs with respect to the vertical TPCs currently used in ND280 [7] is that the new field cage will use a single layer of solid insulator laminated on a composite material, while for the current ND280 TPCs, two gas-tight boxes, one inside the other, were used. This design allows to minimize the dead space and maximize the tracking volume by reducing the distance between the outer TPC wall and the active gas volume from 12 cm to 4 cm. The radiation length of the material composing the field cage is 2%.

In order to test the construction process of the HA-TPCs field cages, several prototypes have been produced and the one, that shares all the characteristics of the final field cages, was used for the test beam described in this paper.

The field cage prototype is built with lightweight and low-Z mechanical structures with an hollow shell shape constituting the box. The box is laminated on an Aluminum mold in several layers, namely Kapton sheets, aramide fiber-fabrics peels and honeycomb spacer panels glued together. The field cage is then enclosed on the two sides with a cathode plane and the anode where the ERAM detector is located.

The innermost cage wall surface embeds a double layer of thin Copper strips: the field strips for degrading the potential from the cathode to the anode and the mirror strips on the opposite side, for regularizing the field nearby the walls and for mitigating the effects of free charge deposition on dielectric surfaces. The strip foils are produced by the CERN Micro-Pattern Technologies service. In order to protect the field cage from the possible presence of tiny carbon fibers embedded into the aramide fiber fabric (Twaron) the mirror strip side is protected with an additional Kapton coverlay glued on it.

The prototype has the same drift length (1 m) as the HA-TPCs and a reduced transverse area (0.42 m $\times$0.42 m) suitable to host one ERAM module. It was produced by the NEXUS company (Barcelona, Spain) and the different phases of the production of the prototype are shown in Fig. 1

Prior to exposing the prototype to the electron beam at DESY, an extensive characterization of the field cage has been done at CERN. The properties were extremely good concerning fiberglass flanges smoothness quality,

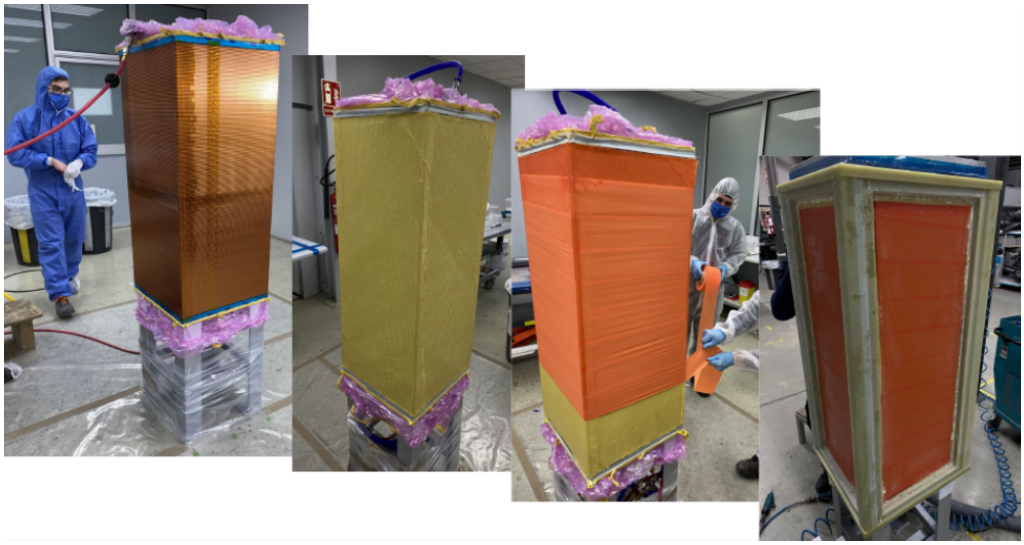

Figure 1: Phases of a field cage prototype production. From left to right: strip foil wrapped onto the mold, aramid fiber fabric (Twaron) glued onto the strip foil layer, Kapton tape wrapped on the Twaron layer before glue curing phase, top and bottom flanges and angular bars applied. The vertical direction in these photos represent the drift direction and the ERAM will be installed on the top surface with the cathode on the bottom.

gas tightness (measured leakage below 0.1 l/h), inner surface quality and deformations smaller than 0.2mm, compatible with prototype mold tolerances. We also performed several measurements of resistance and capacitance on the field and mirror strips showing the electric field is behaving as expected.

2.2. ERAM detector

A description of the ERAM technology and of the detector used for the HA-TPCs of T2K is given in [16]. The ERAM modules built for T2K have a size of 340×420 mm^2 and are segmented in 32×36 rectangular pads of size 11.18×10.09 mm^2.

The ERAMs are used to readout the ionization electrons produced by charged particles crossing the TPC gas volume. These electrons are drifted to the anode readout plane of the TPC under a uniform electric field. On the readout plane, an avalanche is generated by a high electric field in the ERAM amplification region. The resulting pattern of illuminated pads corresponds to the trajectory of the track.

The main difference between the bulk-Micromegas technology used for the existing ND280 TPCs and an ERAM is that, in the case of bulk-Micromegas

and for short drift distances the position reconstruction is limited by the pad size that is larger compared to the avalanche size. In the ERAM, instead, the anode is covered by a foil of insulating material with a thin resistive layer on top, inducing signals over several pads. This allows a better reconstruction of the position of the charged particles crossing the TPC.

The ERAM detector uses a Diamond-Like Carbon (DLC) thin layer sputtered on a 50 µm thick APICAL (Kapton) insulator sheet. The detector installed on the field cage, named ERAM-01, has a resistivity of 300–400 kOhm/□ using DLC foils stack on a 150 µm glue layer.

2.3. HA-TPC electronics

The full electronics chain that will be used for the HA-TPCs has been installed on the ERAM-01 and tested during the test beam described in this paper.

The HA-TPC electronics, the main components are shown at Figure 2, is based on the use of the AFTER chips [17], that had been designed for the existing ND280 TPCs. The AFTER chip is a 72-channel device that includes preamplifiers and shapers with programmable gain and peaking time coupled to a 511-time bucket switched capacitor array (SCA). During the test beam the electronics peaking time was set to 200 or 412 ns.

The Front-End Cards (FEC) have been newly designed and host 8 AFTER chips. They are installed parallel to the ERAM modules and two FECs are used to readout one ERAM (1152 channels). The response linearity of the FEC has been measured with a dedicated campaign and showed a uniform response of all the channels with typical differences in linearity among neighboring pads smaller than 2%.

The two FECs on each ERAM are connected to a Front-End Mezzanine (FEM) card that performs their control, synchronization and data aggregation.

As back-end electronics we used the TDCM, a generic clock, trigger distributor and data aggregator module designed for several projects, including the HA-TPCs.

3. Simulation of the ERAM response

In this paper we will present first comparisons between the data and a Monte Carlo simulation of the ERAM detector. To develop the simulation we benefited from the already extensively verified simulation of the T2K TPCs

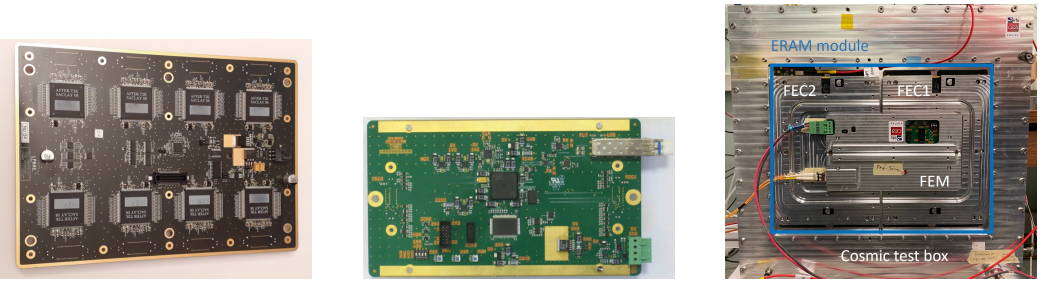

Figure 2: Photo of one FEC with the 8 AFTER chips (left), and of one FEM (center). On the right plot the two FECs are connected to the ERAM module and the FEM is connected on top of both FEC for signal readout.

in the ND280 software [1]. The new feature that was implemented in the model for this work is the resistive layer of the ERAM detectors.

3.1. Simulation framework

The simulation starts from GEANT4 [20] that takes care of simulating the propagation of the charged particles in the TPC gas. To evaluate the energy loss and the produced ionization the PAI model [21] is used with at most a 1 mm computation step. The gas composition is the standard T2K gas [22], a mixture of Ar:CF_4:iC_8H_{10} (95:3:2).

The primary energy deposition by the charged particle is converted into ionization electrons (typically 100 electrons per cm). The ionisation potential for T2K gas is set to 26.8 eV. These electrons are moved to the ERAM plane with the arrival time estimated based on the drift velocity. The electrons are distributed on the sensitive plane following a Gaussian distribution assuming a transversal diffusion of $\sigma_{\text{trans}} = 286\ \mu\text{m}/\sqrt{\text{cm}}$ and a longitudinal diffusion of $\sigma_{\text{long}} = 210\ \mu\text{m}/\sqrt{\text{cm}}$.

For each electron arriving to the ERAM the amplification is simulated based on the ERAM gain G. Fluctuations in the avalanche processes are taken into account by extracting the gain g_e for each electron as $g_e = -\log(1 - \text{uniform}(0,1)) \times G$. The value of G used in the simulation is 1800.

The amplified signal is then given as input to the simulation of the resistive layer that will be introduced in the next section. The resulting signal in each pad is then convoluted with the AFTER electronics response function and digitized with a sampling time of 40 ns.

3.2. Resistive layer simulation.

The behavior of the resistive layer can be approximated to a RC continuous network [23]. In this model, the charge density caused by the point-like electron deposited in $\vec{r_0} = (x_0, y_0)$ ($\rho(\vec{r}, t = 0) = \delta_{\vec{r_0}}(\vec{r})$) is described with the solution of the 2D diffusion equation:

$$\rho(\vec{r}, t) = \frac{RC}{4\pi t} \times \exp\left(-\frac{r^2 RC}{4t}\right) \tag{1}$$

where $r = \sqrt{(x - x_0)^2 + (y - y_0)^2}$ is a distance from the initial charge deposition, t is time and RC is a network characteristic of the ERAM. For our case, ERAM are expected to have an RC within 50-120 ns/mm^2. To compute the observed charge in a given pad the equation above should be integrated over the pad surface

$$\begin{aligned} Q_{unit}(t) = &\int_{x_{min}}^{x_{max}} \int_{y_{min}}^{y_{max}} \rho(\vec{r}, t) dx\, dy \\ =&\frac{1}{2}\pi \left(\text{Erf}\left[\frac{\sqrt{RC}(x_{max} - x_0)}{2\sqrt{t}}\right] - \text{Erf}\left[\frac{\sqrt{RC}(x_{min} - x_0)}{2\sqrt{t}}\right]\right) \\ &\times \left(\text{Erf}\left[\frac{\sqrt{RC}(y_{max} - y_0)}{2\sqrt{t}}\right] - \text{Erf}\left[\frac{\sqrt{RC}(y_{min} - y_0)}{2\sqrt{t}}\right]\right) \end{aligned} \tag{2}$$

where Erf is the error function and x_{min}, x_{max}, y_{min}, y_{max} are pad borders coordinates.

The evolution of the charge in the pad is convoluted with the derivative of the AFTER electronics response:

$$E(t) = \left(\frac{t}{t_p}\right)^3 \exp\left(-\frac{3t}{t_p}\right) \sin\left(\frac{t}{t_p}\right) \tag{3}$$

where t_p is the electronics peaking time. The unit waveform (WF) is then:

$$WF_{unit}(t) = Q_{pad}(t) \circledast \frac{dE}{dt}(t) = \int_{-\infty}^{\infty} Q_{pad}(t - \tau)\frac{dE}{dt}(\tau) d\tau. \tag{4}$$

Finally, when considering an avalanche of electrons, the waveforms induced in each pad by each electron of the avalanche should be computed

taking into account the arrival of each of them and summed in order to obtain the complete waveform WF of the avalanche.

Therefore, the numerical evaluation of the diffusion equation solution and of the convolution are extremely heavy in terms of computation time. To keep the simulation to a reasonable time some approximations were included and described below.

The first method is related to reducing the total number of avalanches to be simulated. The pad is divided into several smaller sub-pad regions e.g. 3×3 or 5×5. All the avalanches that are detected in the same pad sub-region are merged into one and the charge Q is computed for the sum of all the contributions in this sub-pad.

The next and the most significant optimisation is related to the pre-computation of the diffusion equation solution and convolution. Before starting the simulation the detector response is pre-computed for a unit charge, a given RC that is input to the model, and for all the positions across a 2D grid in the pad, $\mathrm{Q_{unit}(RC, x_i, y_i, t)}$, where $\mathrm{x_i}$ and $\mathrm{y_i}$ are the coordinates of a sub-pad center. The step of the grid can be tuned and for this work we divided the pad in a grid of 10×10 sub-pad regions. The obtained distributions are convoluted with the derivative of the electronics response to get the waveform ($\mathrm{WF_{unit}}$) for a unit charge. The final waveform WF(t) can be easily obtained by scaling the pre-computed solution $\mathrm{WF_{unit}}$ with the total charge $\mathrm{Q_i}$ in each sub-pad i obtained from GEANT4, so that:

$$\mathrm{WF(t)} = \sum_{\mathrm{i}} \mathrm{Q_i} \times \mathrm{WF_{unit}(x_i, y_i)(t)}. \tag{5}$$

The main approximation in this computation is the assumption that all the electrons in a sub-pad arrives at the center of this sub-pad. This implies that no numerical computations are needed during the simulation.

Two examples of the resulting WF, one for the data and one for the simulation, are shown in Fig. 3 for the leading and for two neighboring pads. Here and in the following of this paper, the leading pad is defined as the pad with the largest maximum of the waveform while neighboring pads are the ones adjacent to the leading pad in the direction perpendicular to the track (see discussion on clustering algorithms in Sect. 6).

The optimization methods described above allow to reduce the computing time by more than two order of magnitude without impacting the simulation output as it can be seen in Fig. 4 where no differences are observed in the

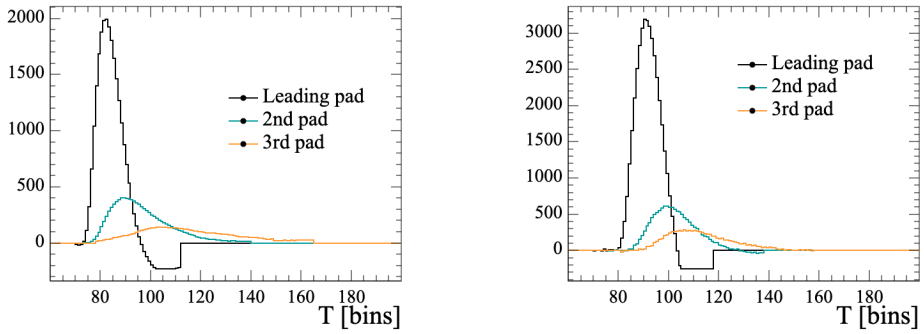

a b

Figure 3: The example waveforms for the leading and adjacent pads in (a) data and (b) MC.

charge ratio and time differences between the leading and the neighbour pad.

4. Characterization of ERAM detector

Each ERAM detector is scanned after the production on an X-ray test bench at CERN. The test bench consists into a chamber with a 3 cm width and is equipped with a robotic X-Y-Z arm system on an optical breadboard of 120×60 cm^2 holding a 250 MBq ^{55}Fe source emitting 5.9 keV photons that deposit all their energy in the gas.

A 1.5 mm diameter collimation hole in front of the source assures that the majority of photo-electrons arrives on the targeted pad. Prior to the scan, the ERAM is aligned to ensure the position of the source with respect to the center of each pad.

Each channel of the ERAM is scanned for ∼3 minutes at a rate of 100 Hz, allowing to reconstruct the spectrum of the ^{55}Fe source and compute the gain for each pad. The map of the gain on the ERAM-01 and the gain uniformity are shown in Fig. 5.

The data from the test bench can also be used to measure the RC uniformity of the ERAM. This measurement campaign will be subject of a future publication. For the comparisons between data and simulations that will be presented in this paper, we assume uniform gain and RC in the simulation.

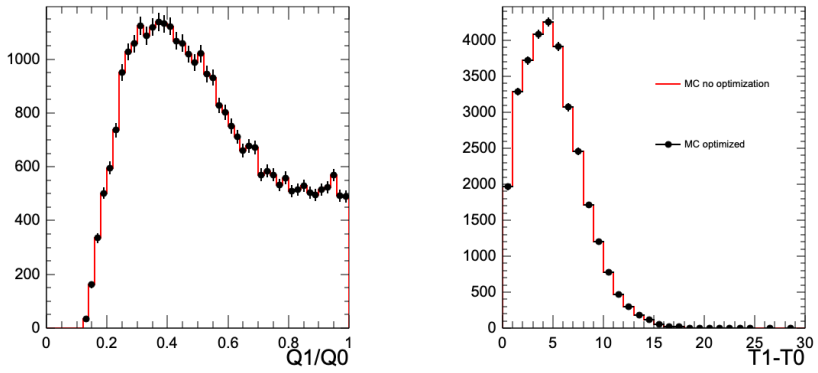

Figure 4: Charge ratio (left) and time difference (right) between leading and neighbour pad with and without the optimization needed to reduce computation time.

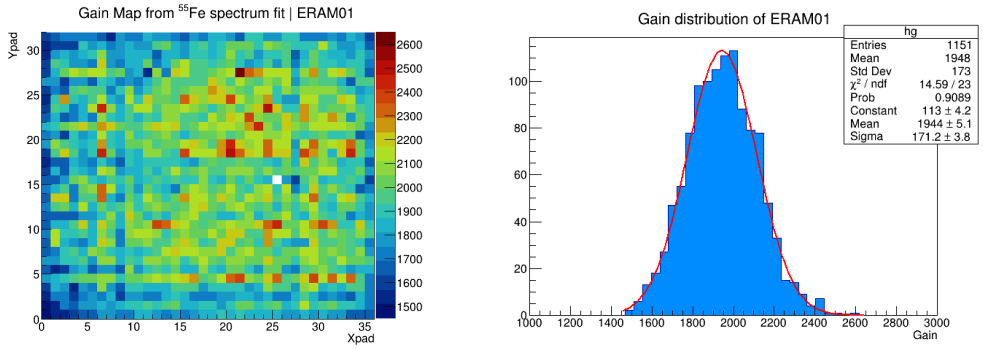

a b

Figure 5: Map of the gain (a) and gain distribution (b) obtained with an ^{55}Fe source for the ERAM used in the test beam.

5. Collected Data at DESY

The tests at DESY were aimed to ensure that the HA-TPC prototype design fully satisfies the requirement of the ND280 upgrade for drift distances up to 1 m that corresponds to the maximum drift length of the HA-TPC. Therefore, this test beam cover all the possible conditions of the final HA-TPC.

The High-Angle TPC prototype equipped with ERAM-01 was filled with T2K gas mixture and tested at DESY T24/1 facility. The chamber was

placed inside the PCMAG solenoid providing a magnetic field up to 1.25 T and exposed to the electron beam with tunable momenta between 1 and 4 GeV/c. The solenoid is equipped with a movable stage that allows moving the detector along the horizontal and vertical directions, and rotating ±45 degrees around a vertical axis. The TPC holder can be manually rotated inside the magnet.

Most of the data were taken with the cathode High Voltage set at 26.7 kV corresponding to an electric field in the TPC of 275 V/cm. In order to test the setup parameters and configuration, various scans were performed.

The PCMAG movable stage allows to perform scans in X (along the beam) and Y (perpendicular to the beam) directions as well as scans in Z (drift distance). This is particularly interesting because allows to check the impact on the performances of possible non-uniformities in the gain or in RC.

The drift distance scan was done for two values of the electronics peaking time of 412 ns and 200 ns.

The data were also collected for different rotation angles around the horizontal (ϕ angle) axis, within varying magnetic fields and for three drift distances, one close to the ERAM, one in the middle of the chamber, and one close to the cathode.

6. Reconstruction algorithms

Both, simulated and test beam tracks were reconstructed with the same analysis framework that uses DBSCAN [24] algorithm and the PRF method (discussed in Sect. 8)

The track is composed by "clusters" that are group of pads in the direction perpendicular to the track.

In order to be selected, a track needs to cross the whole detector without breaks or splits. A split is defined as the case where there is more than one cluster in a given column. An event containing a split is considered as a multiple track candidate and is rejected in our analysis. However, due to the large multiplicity (number of pads per cluster) induced by the ERAM, two close parallel tracks may not be separated by a gap and thus mis-reconstructed as one single track.

To reject such a topology and also to remove superimposed tracks, a cut on the mean number of pad per cluster (multiplicity) of the track is applied. This cut depends on the track clustering algorithm that is used

to reconstruct the tracks. As it was introduced in [16], we use horizontal and vertical clustering for tracks with incident angles below 30 degrees and above 60 degrees respectively, while for inclined tracks we use a diagonal clustering algorithm in which pads are combined into clusters according to their diagonal.

The mean multiplicity depends on the reconstruction algorithm and on the peaking time for the electronics. It is shown in Fig. 6 for horizontal and inclined tracks at small and large drift distance. For large drift distances and for inclined tracks the multiplicity tends to increase due to the transverse diffusion of the electrons while crossing the gas volume. For horizontal tracks, instead, this effect is hidden by the larger effect induced by RC.

For the analyses presented in this paper we select tracks with mean multiplicity smaller than 3.4 for horizontal tracks and 2.2 for diagonal tracks with 200 ns peaking time. For 412 ns peaking time only horizontal tracks were taken and, for this sample, we required a mean multiplicity smaller than 4.3.

Finally, to avoid edge effects, the pads at the border are excluded from the reconstruction and hence horizontal tracks have 34 clusters while vertical tracks have 30.

7. ERAM response in data and simulation

To validate the simulation described in Sect.3, we produced electrons propagating in the Y direction and we compared some variables describing the ERAM response, including charge sharing and time differences between neighboring pads in data and simulation. These comparisons are done also with respect to the data taken at DESY in 2019 with a different ERAM module that is described in [16]. The comparison between data and simulation for spatial resolution and dE/dx resolution will be shown in Sect. 10.

The most significant variables for the resistive feature characterisation are the charge ratio and the time difference between the WFs observed in the adjacent pad and the ones in the leading pad.

For these comparisons, the charge in the pad is defined as the maximum of the waveform and the time is defined as the time bin at which the waveform was maximum. The pads in a cluster are then ordered according to their charge (Q_1 and T_1 refer to the pad with the largest charge, Q_2 and T_2 the second, Q_3 and T_3 the third).

Since these variables depend on the relative position of the track and the pad, we sampled the distributions based on the reconstructed track position.

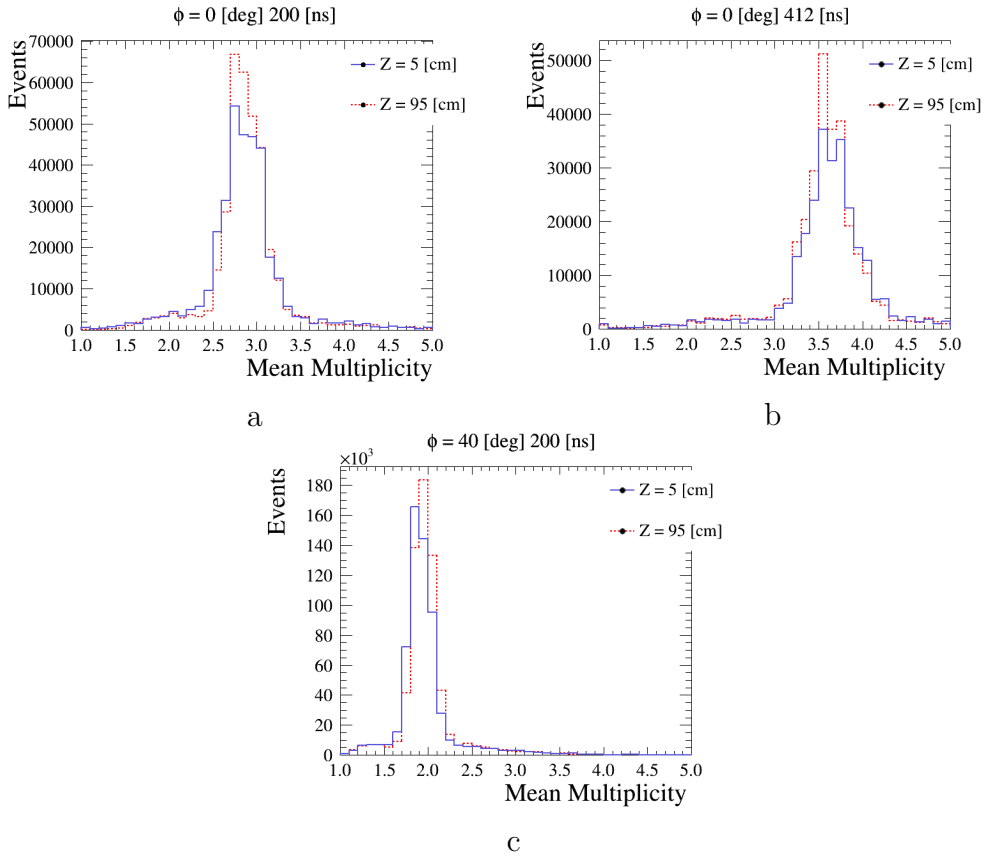

Figure 6: Mean multiplicity at different peaking time for (a,b) horizontal and (c) inclined tracks at small and large drift distances.

These distributions are shown in Fig. 7 for 5 cm drift distances.

In order to make a more quantitative comparison between data and Monte Carlo, the distributions of Figs. 7 were fit with the Landau function and the most probable value (MPV) is plotted in Fig. 8 for these data (DESY 2021), the one from the previous test beam (DESY 2019) and MC samples generated with with RC=55 ns/mm^2 and RC=100 ns/mm^2.

The comparison clearly shows the different behaviour of the two ERAM modules, especially for what concerns the time differences that are most affected by RC.

The difference in the data can be explained by a different value of RC between the two modules. The data from 2021 are better reproduced by using RC=100 ns/mm^2, however, even for this RC value, some visible differences

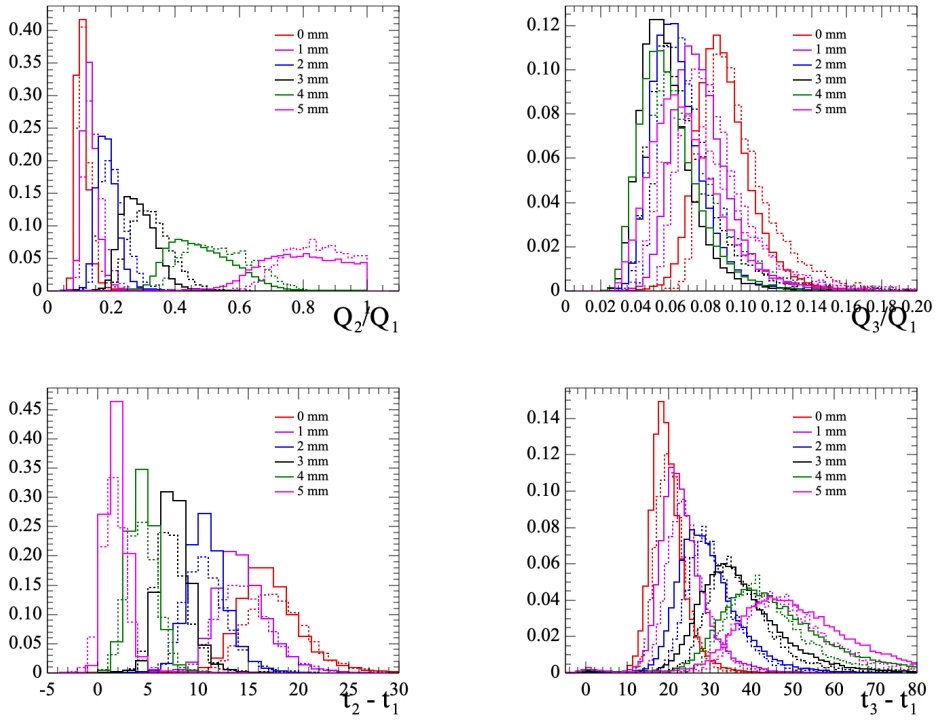

Figure 7: Ratio of the charge in the second pad (top left) and third pad (top right) with respect to the leading pad and time difference between first and second pad (bottom left) and first and third pad (bottom right). The solid lines represent data (DESY 2021) and the dashed ones the simulation.

between the data and simulation are observed. As we will show in Sect. 10, these differences do not affect the detector performances in terms of spatial or energy resolution.

The charge ratio and time differences for larger drift distances, where effects induced by the diffusion in the gas play an important role, show in general a better agreement between data and simulation as shown in Fig. 9.

For the future, we expect to improve the agreement between data and simulation by using in the simulation the value of RC that will be measured with the Test Bench described in Sect. 4 and taking into account possible non-uniformities within the detector.

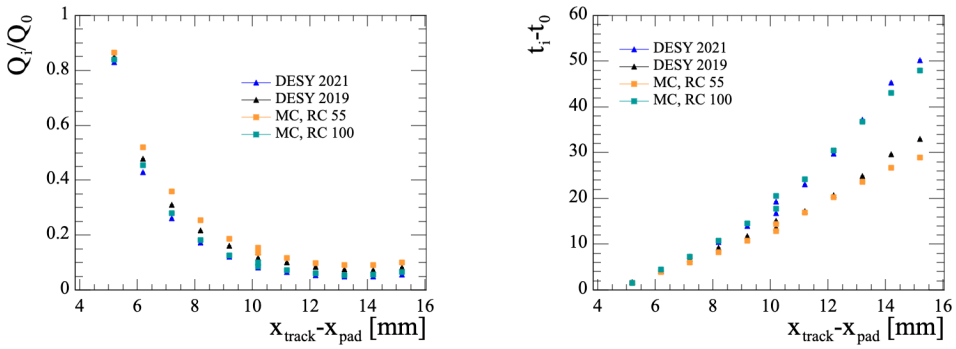

a b

Figure 8: The comparison of the MC simulations and two test beams (DESY 2021 and DESY 2019) for the charge ratio (a) and time difference (b) between leading and adjacent pads as a function of the difference between pad centre (x_{pad}) and reconstructed track position (x_{track}). Two points are shown for $x_{track} - x_{pad} = 10$ mm because, for tracks in the center of the pad, the two adjacent pads have the same distance from the track.

8. Spatial resolution

The ND280 TPCs measure the momenta of the outgoing particles from neutrino interactions allowing to reconstruct the energy of the incoming neutrino, one of the critical element to precisely measure neutrino oscillations parameters.

The TPC momentum resolution depends on the spatial resolution [25] that can be characterized with test beam data. For this analysis, the spatial resolution is measured by employing a "pad response function" (PRF) in the same manner as in [15, 16].

In this method we define, for each cluster, the residual as the difference between the position of the track reconstructed locally (e.g. in one column) and the position according to the fit of the track. The distribution of the residuals in each cluster is fitted with a Gaussian and its width represents the spatial resolution.

The measurement of the track position is performed with an iterative procedure. For the first step, all the tracks are reconstructed using the charge barycentric method. Such a method estimates the position of the track in a certain cluster by weighting the centre of the pad position by the charge in this pad. The estimated primary track positions in each cluster are then fit with a parabola over the whole detector (global fit). Based on the results of the fit, a pad response function scatter plot is filled for each pad. PRF

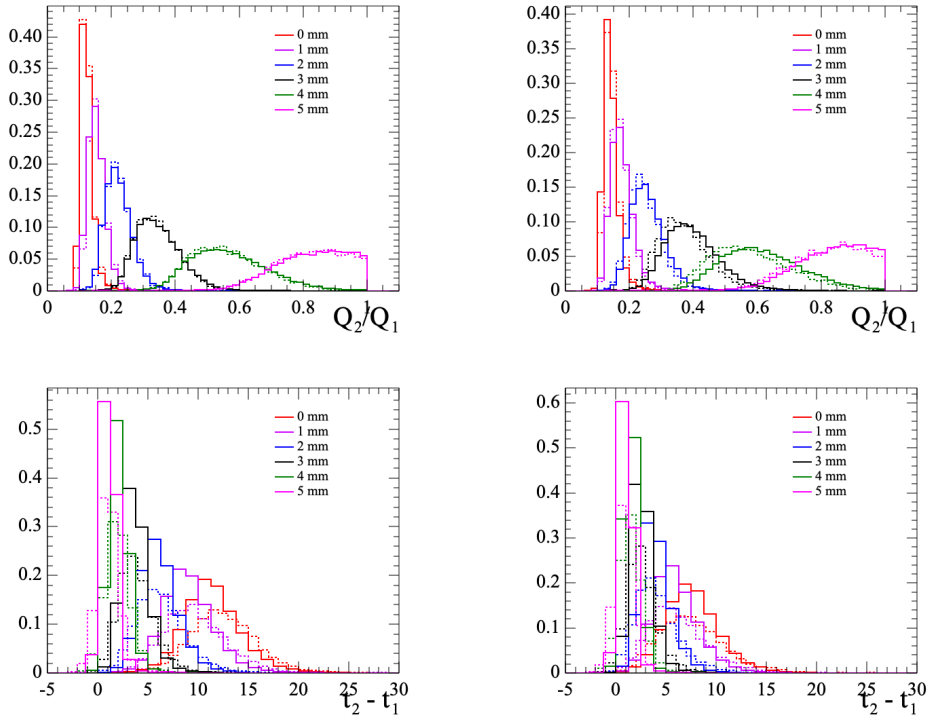

Figure 9: Charge ratio between second and leading pad for drift distances of 50 cm (top left) and 90 cm (top right) and time difference between first and second pad for drift distances of 50 cm (bottom left) and 90 cm (bottom right) . The solid lines represent data (DESY 2021) and the dashed ones the simulation.

function is defined as:

$$\mathrm{PRF}(\mathrm{x_{track}} - \mathrm{x_{pad}}) = \mathrm{Q_{pad}}/\mathrm{Q_{cluster}} \tag{6}$$

where $\mathrm{x_{track}}$ and $\mathrm{x_{pad}}$ are positions of the track from the global fit and the center of the pad respectively and $\mathrm{Q_{pad}}$ and $\mathrm{Q_{cluster}}$ are charges collected by the pad and by the whole cluster.

The PRF scatter plot is fitted with a ratio of two polynomes (the same as in [16, 26]). The scatter plot and the parametrization of the PRF are done independently for samples at different drift distances and inclination. The estimated parameters of the PRF analytical function are used further in the χ^2 minimization procedure to estimate the track position in each cluster.

$$\chi^2 = \sum_{\text{pads}} \left(\frac{\mathrm{Q_{pad}/Q_{cluster}} - \mathrm{PRF(x_{track} - x_{pad})}}{\sigma_{\mathrm{Q_{pad}/Q_{cluster}}}} \right)^2 \tag{7}$$

where $\sigma_{\mathrm{Q_{pad}/Q_{cluster}}} = \sqrt{\mathrm{Q_{pad}/Q_{cluster}}}$.

In the following iterations the track position was evaluated from the fit. The iteration procedure is repeated while the spatial resolution keeps improving and it typically converges after three iterations. An example of PRF for horizontal and inclined tracks is shown in Fig. 10. A small dip around zero can be observed in PRF for inclined tracks. This is due to the width of the distribution around zero and to the freedom of the polynomial fit.

The spatial resolution was defined as a mean of the residual distribution for each cluster. An example for horizontal and inclined tracks is shown in Fig. 11. The distribution is expected to be centered at zero and differences with respect to zero are the biases that will be discussed in Sect. 8.3.

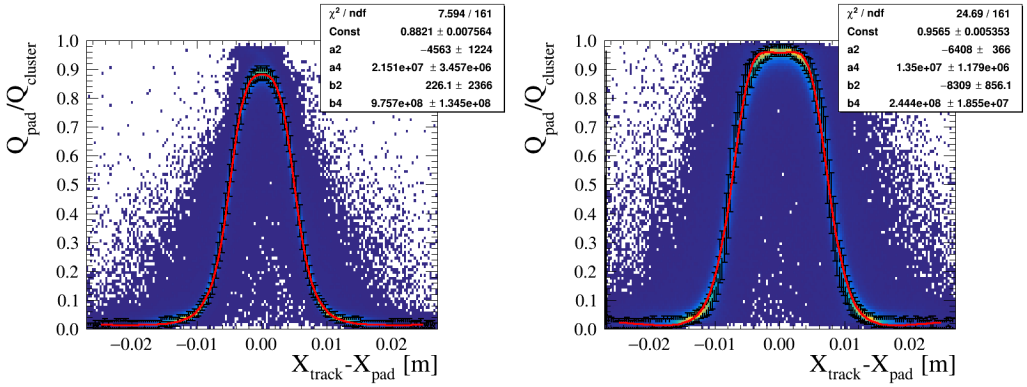

Figure 10: PRF function for (a) horizontal and (b) inclined tracks.

8.1. Spatial resolution for horizontal tracks

With this method we can evaluate the spatial resolution for different topologies of track. The results for the horizontal tracks as a function of the drift distance for different electronics peaking time are presented in Fig. 12.

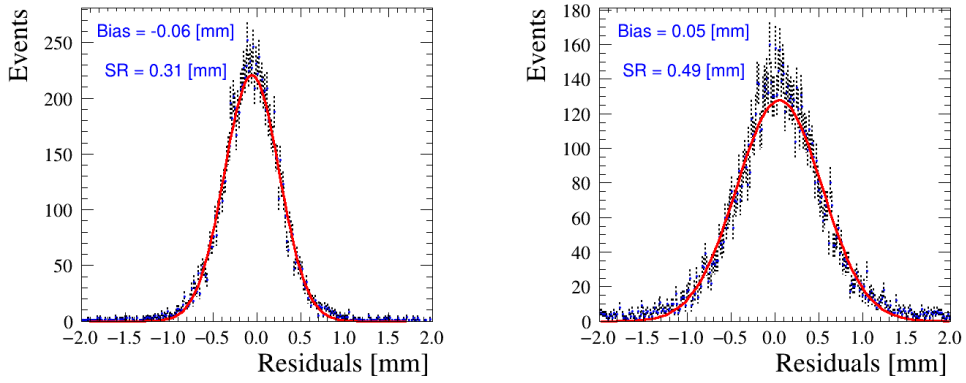

a b

Figure 11: Residuals distribution for single cluster for (a) horizontal and (b) inclined tracks.

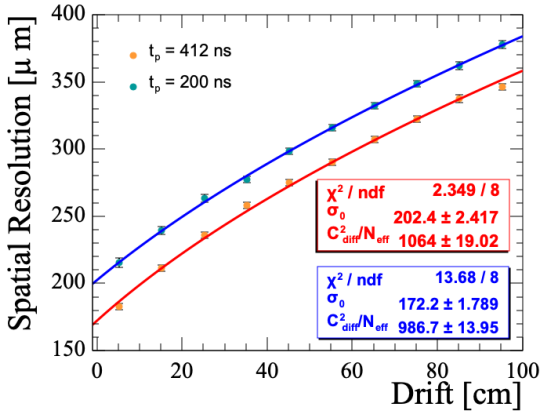

Figure 12: Spatial resolution with respect to the drift distance for the beam parallel to the pad side with a magnetic field of 0.2 T, drift velocity of 78.7 mm/μs and peaking times of 200 ns and 412 ns.

The dependence of the resolution over the drift distance is expected to follow

$$\sigma(\mathrm{Z}) = \sqrt{\sigma_0^2 + \mathrm{C}_{\mathrm{diff}}^2/\mathrm{N}_{\mathrm{eff}} \times \mathrm{Z}} \tag{8}$$

where σ_0 is a resolution at null drift distance, $\mathrm{C}_{\mathrm{diff}}$ is a transversal diffusion constant and $\mathrm{N}_{\mathrm{eff}}$ is a number of effective electrons [27]. The observed

dependence is in agreement with this law. The peaking time mildly affect the C^2_{diff}/N_{eff} term, but changes the σ_0. A larger peaking time results in a higher amplitude in the neighbour pads. Thus we have more robust information for the PRF fit and the track position reconstruction is more precise.

The spatial resolution can also depend on the ERAM module characteristics, such as its gain and the local RC value. To check for these possible dependencies we used a scan done at fixed drift distance but with horizontal tracks crossing the ERAM at different X positions and vertical tracks crossing the ERAM at different Y positions. The spatial resolution obtained for the different X and Y position is shown in Fig. 13. No large differences are observed indicating that possible local non-uniformities on the ERAM module do not play a dominant role in the detector performances.

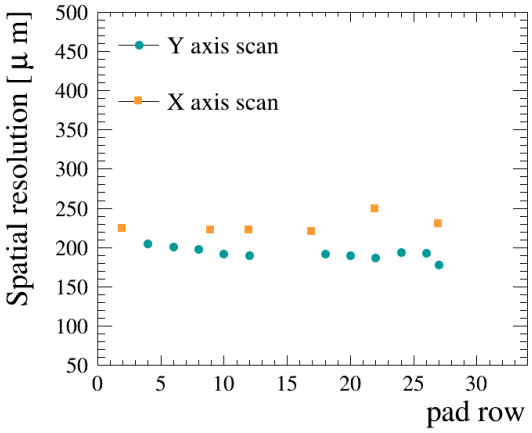

Figure 13: Spatial resolution versus different Y and X position at 412 ns peaking time.

8.2. Spatial resolution for inclined tracks

The collected test beam data allows studying spatial resolution as a function of the angle of inclination of the tracks within the ERAM module plane. The novelty with respect to the studies performed in [16] is that we could evaluate the spatial resolution performances for inclined tracks at long drift distances. The results are presented in Fig. 14 (a), where angles from 0 to 30 degrees and from 70 to 90 clusters are defined perpendicular to the track direction (horizontal/vertical fit), and for the highly inclined tracks, with the angle between 40 and 60 degrees, the clusters defined along the diagonals as

described in the section 6. In [16] it has been shown that the use of a diagonal fit for highly inclined tracks significantly improves the spatial resolution with respect to the use of horizontal or vertical fits.

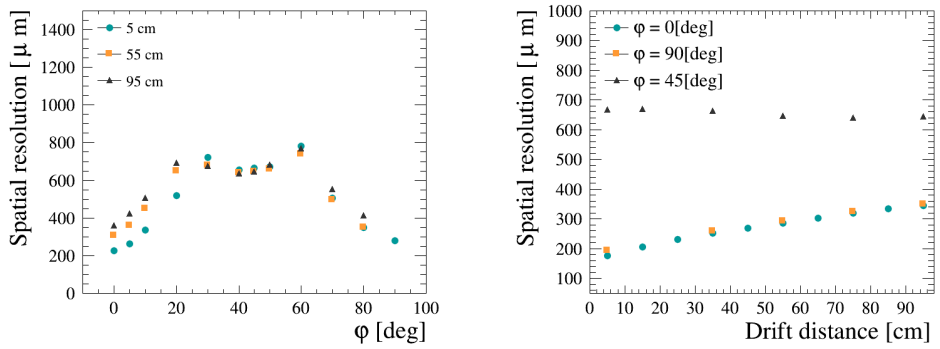

a b

Figure 14: Spatial resolution versus different angles of the electron tracks inclination in the pad plane with 200 ns peaking time, 0.2T magnetic field and for various drift distances: 50 mm, 550 mm, 950 mm (a) and spatial resolution versus drift distance for horizintal (0 deg.), inclined (45 deg.) and vertical (90 deg.) tracks.

Fig. 14 a demonstrates that, while the spatial resolution depends on the angle, it stays between 200 and 800 μm for all the analyzed samples. In particular, it is interesting to notice at Fig. 14 b that, while the spatial resolution degrades with the drift distance for horizontal and vertical tracks, it is constant for inclined tracks. It should be noted, however, that the data at small drift distance had been taken also at different Y (see Fig. 13) and they are not directly comparable with the data taken at same angle but larger drift distances.

The behavior for diagonal tracks can be understood considering that the spatial resolution depends on the charge spread over a certain amount of pads (multiplicity). A diagonal clustering algorithm leads to a smaller mean multiplicity than in the case of horizontal/vertical fit as it was shown in Fig. 6. With the diagonal fit pad size becomes effectively $\sqrt{2}$ times larger, thus degrading the spatial resolution but also making the effect of the transverse diffusion less significant.

Moreover, diagonal fit implies a dependence of the resolution on the length of the track in the cluster. This cause an oscillatory behavior in the spatial resolution versus the cluster that is shown in Fig. 15 a. Fig. 15 b shows

the dependence of the spatial resolution on the track length per cluster for inclined tracks. It is clearly seen that, as expected, the resolution improves for longer track lengths within the cluster.

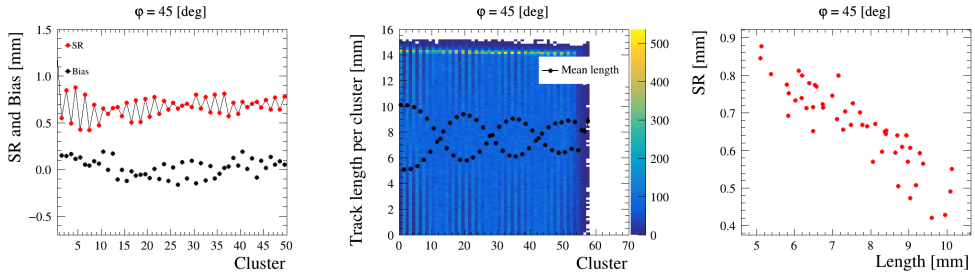

a b c

Figure 15: Tracks of 45 degrees inclination: spatial resolution per cluster (a), track length per cluster (b), mean track length with respect to spatial resolution (c).

8.3. Biases in spatial resolution

The bias of the track position in each cluster of the ERAM pad plane is defined as the mean of the gaussian of the distribution of residuals per cluster, and can be referred to as the systematic uncertainty of the track position estimation. In [16, 28] it is shown that the biases depend on the track position. The data collected during this campaign allow a deeper study of biases, in particular their dependence on drift distance for both horizontal and inclined tracks, as well as their behavior in various magnetic fields (see Sec. 9).

Fig. 16 a shows the bias as function of the drift distance for horizontal tracks. In this figure, the bias is defined as the mean of the absolute values of the biases per cluster. It is observed that biases are larger at short and long drift distances than at distances corresponding to the middle of the drift volume.

For inclined tracks, instead, as shown in Fig. 16 b, the biases do not depend on the drift distance or on the phi angle of the tracks reconstructed using diagonal clustering.

In order to further investigate the behavior of Fig. 16, the dependence of the spatial resolution and bias per column on the drift distance is shown in Fig. 17. For the smallest and largest drift distances, biases have visible patterns with large and opposite biases at the beginning and at the end of the track. This pattern is not observed for tracks in the center of the ERAM.

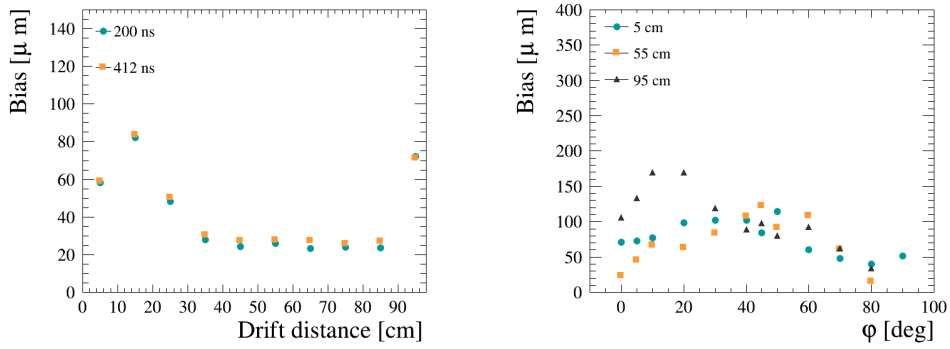

a b

Figure 16: Track position bias with respect to the drift distance for the beam parallel (a) and inclined (b) to the pad side with a magnetic field of 0.2 T, drift velocity of 78.7 mm/μs and peaking time of 200 ns.

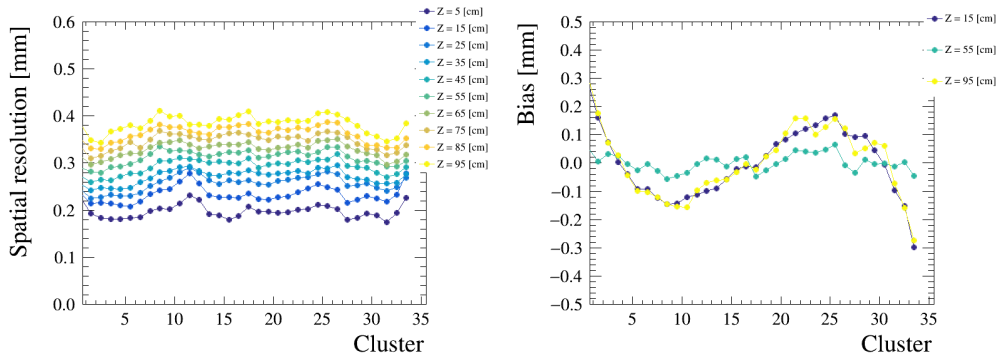

a b

Figure 17: Spatial resolution (a) and track position bias (b) distributions per cluster for the beam parallel to the pad side with a magnetic field of 0.2 T, drift velocity of 78.7 mm/μs and peaking times of 200 ns at various drift positions (z axis).

The observed dependencies of the biases are not observed in the simulation and can point to effects related to non-uniformities in the magnetic field and the E×B effect. In Sect. 11 we will discuss the impact of these effects on the observed tracks, together with a study of the observed biases as a function of the applied magnetic field.

In general the biases are small for all the angles of track inclination ($<$ 200 μm) and their size is negligible for highly inclined tracks.

9. Deposited energy resolution

The other main goal of the HA-TPC is to perform particle identification by measuring the deposited energy by charged particles crossing the gas. The TPC particle identification power will depend on the dE/dx resolution that can be evaluated with the data from this test beam.

In the context of T2K it is particularly important to be able to distinguish electrons and muons. Such an effort is crucial to estimate electron neutrinos contamination in the muon neutrino spectra and predict the un-oscillated amount of the electron neutrino in the far detector. To distinguish electrons and muons the deposited energy resolution requires to be better than 10 % to achieve a more than 3σ separation between electrons and muons.

The deposited energy is calculated per track using the truncated mean method already introduced in [16].

The method consists in calculating the track mean deposited energy by summing the deposited energy in the reduced number of clusters fired by the electron and ignoring the fraction of those that have a large energy contribution. Such contribution is caused by fluctuations in the ionization processes and leads to the smearing of the energy spectrum.

The truncation factor is optimized with the data and we found it to be 0.7 which is the same as for DESY test beam data of 2019 [16]. This means that 70% of the clusters are kept for deposited energy calculations.

The deposited energy per cluster was calculated by taking the maximum of the sum of the waveforms of the pads constituting the cluster. Various charge cluster definitions were studied in [16] and it was shown that the charge defined using the sum of the waveforms results in a better deposited energy resolution.

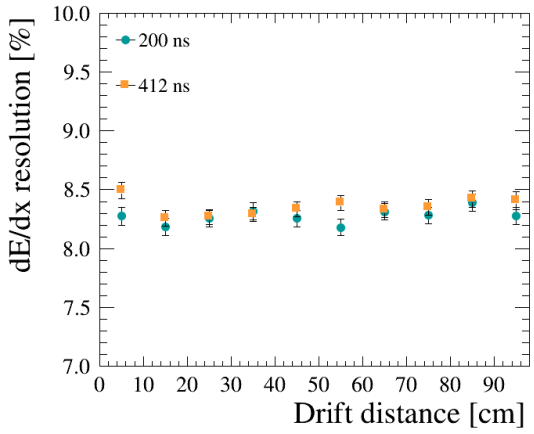

Figure 18: dE/dx resolution with respect to the drift distance for the beam parallel to the pad side with a magnetic field of 0.2 T, drift velocity of 78.7 mm/μs and peaking times of 200 ns and 412 ns.

The deposited energy resolution was measured for both parallel and inclined tracks with respect to the pad side. Fig. 18 shows the deposited energy resolution measured for the parallel tracks for various drift distances.

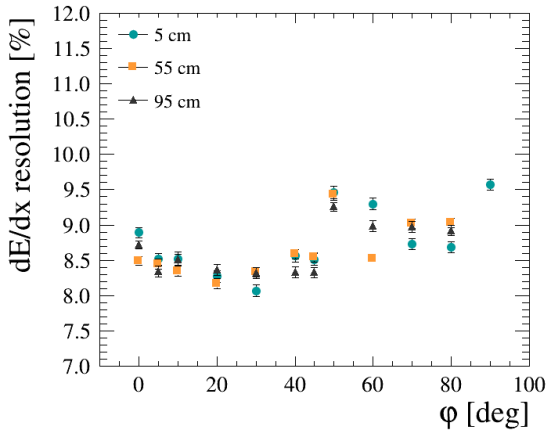

Figure 19: Deposited energy resolution versus different angles of the electron tracks inclination in the pad plane with 200 ns peaking time, 0.2T magnetic field and for various drift distances: 50 mm, 550 mm, 950 mm.

Fig. 19 shows the dE/dx resolution at various drift distances as a function

of the angle within the pad plane.

Additionally, the deposited energy in tracks reconstructed with the diagonal fit were corrected for the track length in each cluster. Such correction accounts for the non-linear dependence of the charge with respect to the track length caused by the charge contribution from the neighbouring clusters for short track cluster length.

The study shows that dE/dx resolution is ∼8.5% for horizontal tracks and stays between 7.5 % and 9.6% for inclined and vertical tracks. Furthermore, it is independent of drift distance and of the electronics peaking time. It has been observed that dE/dx resolution is controlled by balancing two factors: the mean charge per cluster and the number of clusters. Fig. 19 shows that dE/dx resolution worsens for the angles > 45 degrees since for such angles a smaller number of clusters is reconstructed per track due to the rectangular shape of the ERAM.

Finally, as in the case of the spatial resolution, we looked for effects due to non-uniformities of the ERAM by using the X and Y scans. The results are show in Fig. 20. We observe some differences, possibly due to non-uniformities in the gain of the ERAM, but in general the resolution is below 10% for all the Y and X scans.

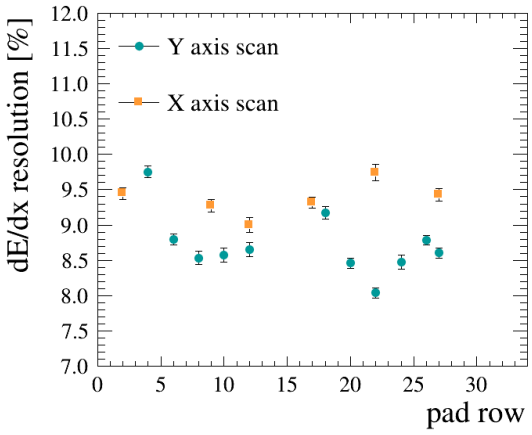

Figure 20: dE/dx resolution for tracks entering the ERAM at different X and Y positions.

The observed results prove that the ERAM energy resolution fulfills the requirements for the ND280 upgrade.

10. Comparison between data and simulation

In this section we compare the performances of the ERAM for spatial and dE/dx resolution between data and simulation.

Fig. 21 shows the spatial resolution for the data and MC samples as a function of the drift distance. The dependence over the drift distance was found to be slightly different using the default value used in the ND280 simulations of the vertical TPC that has a transverse diffusion $\sigma_{\text{trans}} = 286\ \mu\text{m}/\sqrt{\text{cm}}$. The diffusion can be affected by the magnetic field configuration as well as environmental conditions such as temperature and pressure.

We made simulations with different values of σ_{trans}. As expected, in general, increasing σ_{trans} results in a worst spatial resolution for large drift distances. A satisfactory agreement was found by increasing the transverse diffusion by 8%, changing it to $\sigma_{\text{trans}} = 310\ \mu\text{m}/\sqrt{\text{cm}}$. Furthermore, while in the data we observe a dependence on the drift distance in good agreement with the one expected from Eq. 8, in the simulation we observe that this dependence is linear. The origin of this difference between data and simulation is under investigation.

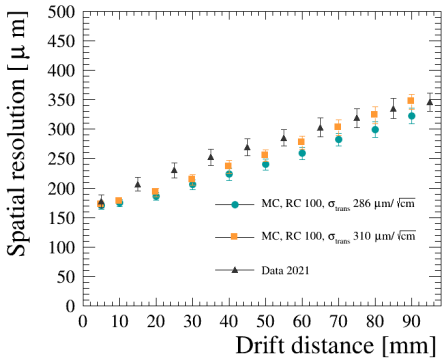

Figure 21: Spatial resolution over the drift distance for DESY data 2021 and MC samples with different values for transversal diffusion.

In Fig. 22 we show the comparison in the spatial resolution between data and simulation for tracks at different angles. For completeness we make the comparison using both, 2019 and 2021 data. It should be noticed that the ϕ scan was done using different electronics peaking times and we did the simulation for the two cases. The simulation correctly reproduces the behaviour observed in the data.

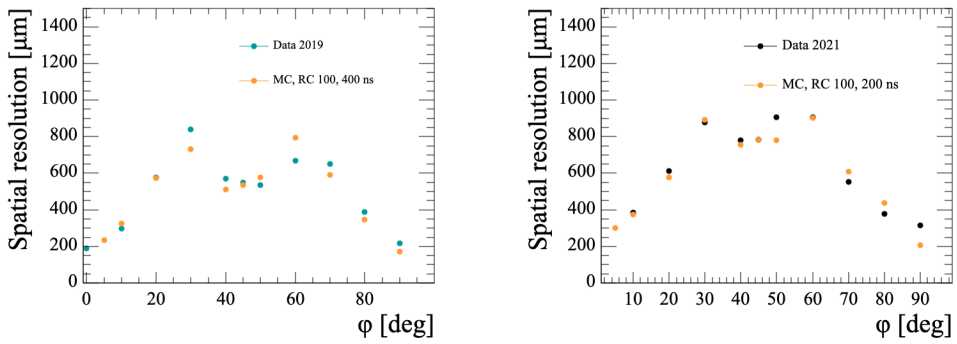

a b

Figure 22: Spatial resolution over angle with respect to pad borders for data and MC samples. The data and MC samples use the following peaking time settings: (a) 400 ns for MC and 412 ns for data 2019 and (b) 200 ns for both MC and data 2021.

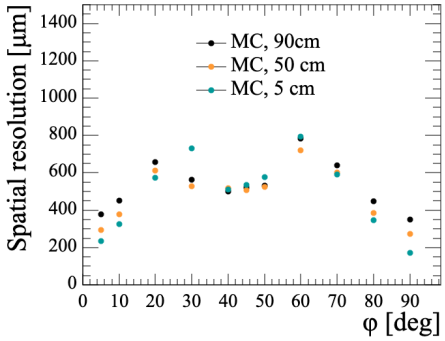

Figure 23: Spatial resolution as a function of the angle with respect to pad borders in the simulation for the different drift distances.

Finally, in Fig. 14 b it was found that the spatial resolution weakly depends on the drift distance for the highly inclined tracks. This effect was cross-checked and confirmed with the simulation. Fig. 23 shows large effect of the drift distance on the tracks close to 0° and 90°, but much smaller effect at 45°.

Finally, Fig. 24 shows the impact on the simulation of a different value of RC. The spatial resolution slightly degrades when RC increases but the effect is within $\sim 10\%$.

Concerning the deposited energy resolution, the simulation reproduces reasonably well the data for both, horizontal and inclined tracks as shown in Fig. 25.

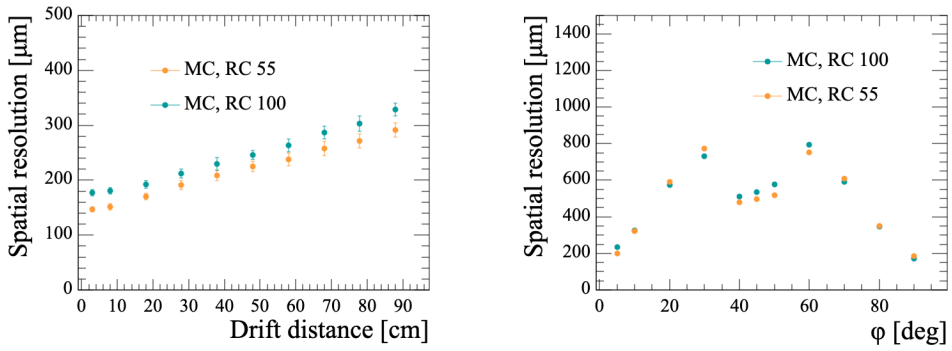

a b

Figure 24: Spatial resolution versus drift distance and angles for simulations generated with different RC

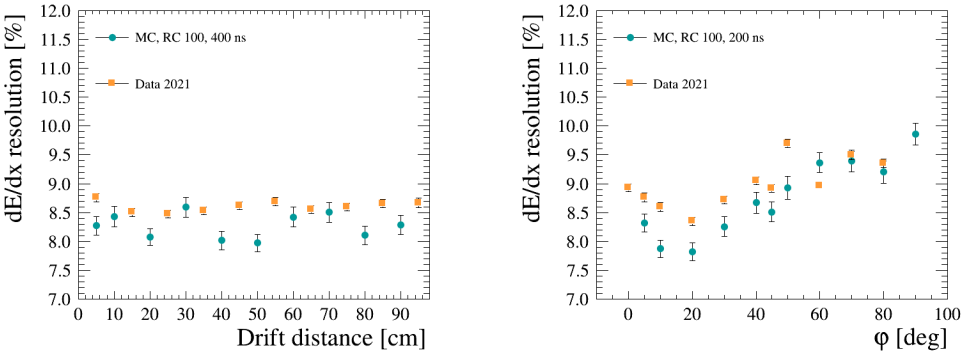

a b

Figure 25: dE/dx resolution in data 2021 and MC for (a) horizontal tracks (at 412 ns peaking time) as a function of the drift distance and for (b) inclined tracks (at 200 ns peaking time) as a function of the track angle inclination.

11. E × B

Inhomogeneities in the magnetic field can create distortions of the image of the track projected on the ERAM. These distortions are not expected to impact the spatial resolution that is computed based on the track image on the ERAM, but can affect the determination of the reconstructed momentum. This effect is expected to be small in ND280, where the magnetic field inside the magnet has been measured with a dedicated campaign [1], and can be larger in the PCMAG used in DESY, where inclined tracks were observed even for horizontal beam as shown in Fig. 26.

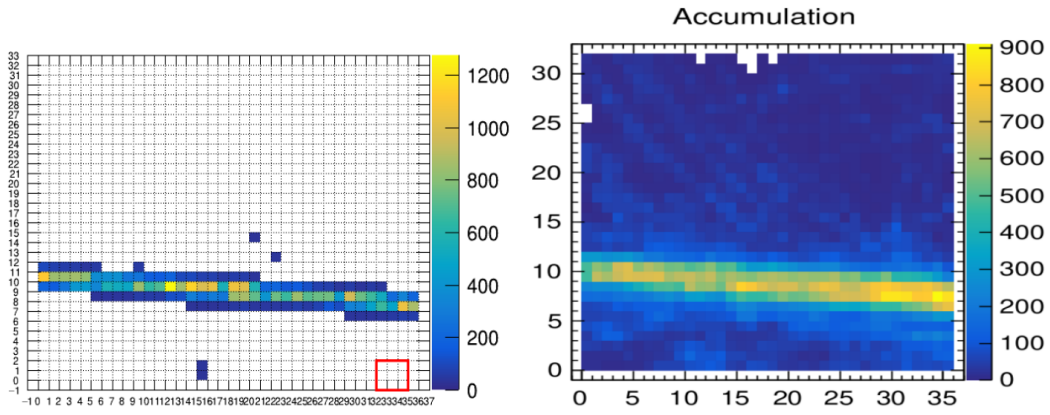

(a) Single event (b) Accumulation of tracks in the dataset

Figure 26: Event display of nominally horizontal tracks. (a) single horizontal track; (b) accumulation plot of the tracks from the same dataset (B = 0.2 T).

It is worth saying that this effect cannot be explained by the curvature induced by the magnetic field that is negligible for the operational magnetic field and electron momenta used in the test beam.

Compelling arguments support the hypothesis of "E × B effect" accounting for the inclination of tracks projected on the ERAM. Below we present the explanation of the effect. The drift velocity is given by the Langevin equation:

$$\vec{\mathrm{V}}_{\mathrm{d}} = \frac{\mu}{1+(\omega\tau)^2}\left(\vec{\mathrm{E}} + (\omega\tau)\frac{\vec{\mathrm{E}}\times\vec{\mathrm{B}}}{|\vec{\mathrm{B}}|} + (\omega\tau)^2\frac{\vec{\mathrm{B}}\cdot(\vec{\mathrm{E}}\vec{\mathrm{B}})}{|\vec{\mathrm{B}}|^2}\right), \tag{9}$$

where $\mu = \frac{\mathrm{e}}{\mathrm{m}}\tau$ is the electron mobility in the gas, $\omega = \frac{\mathrm{eB}}{\mathrm{m}}$, and τ is the time between two collisions.

The scheme visualizing the drift velocity components is shown in Fig 27, in which we have defined the components of $\vec{\mathrm{V}}_{\mathrm{d}}$ as $\vec{\mathrm{V}}_0 = \frac{\mu}{1+(\omega\tau)^2}\vec{\mathrm{E}}$, $\vec{\mathrm{V}}_1 = \frac{\mu}{1+(\omega\tau)^2}\cdot(\omega\tau)\frac{\vec{\mathrm{E}}\times\vec{\mathrm{B}}}{|\vec{\mathrm{B}}|}$ and $\vec{\mathrm{V}}_2 = \frac{\mu}{1+(\omega\tau)^2}\cdot(\omega\tau)^2\frac{\vec{\mathrm{B}}\cdot(\vec{\mathrm{E}}\vec{\mathrm{B}})}{|\vec{\mathrm{B}}|}$. The angle between the electric and magnetic field is defined as δ so that $|\vec{\mathrm{E}}\times\vec{\mathrm{B}}| = \mathrm{EB}\sin(\delta)$.

Assuming small δ we can use $\cos\delta = 1$ and $\sin\delta = \delta$. In this assumption the $\vec{\mathrm{V}}_2$ component aligns with the electric field ($\vec{\mathrm{V}}_0$ component). $\vec{\mathrm{V}}_1$, is perpendicular to $\vec{\mathrm{V}}_0$ and $\vec{\mathrm{V}}_2$. The track displacement angle ϕ is then given by:

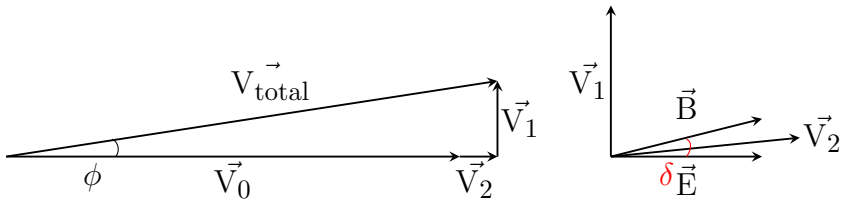

Figure 27: Schematic view of the drift velocity components according to the Lagevin equation.

$$\phi = \text{atan}\left(\frac{\vec{V}_1}{\vec{V}_0 + \vec{V}_2}\right) = \text{atan}\left(\frac{(\omega\tau)\frac{\vec{E}\times\vec{B}}{|\vec{B}|}}{E + (\omega\tau)^2\frac{\vec{B}\cdot(\vec{E}\vec{B})}{|\vec{B}|}}\right) = \text{atan}\left(\frac{\delta\omega\tau}{1+(\omega\tau)^2}\right) \tag{10}$$

As it can be seen in Fig. 26, the electrons drifting to the leftmost region of the ERAM are shifted upwards, while the ones drifting to the rightmost region are shifted downwards, with the magnitude of this vertical displacement given by Eq. 10. From Eq. 10 it can also be seen that the E×B effect is stronger for moderate magnetic field (around 0.2-0.4 T) and weaker for the strong magnetic field. Fig. 28 shows the dependence of the apparent track inclination on magnetic field, superimposed to the theoretical prediction of equation 10, where the parameter δ is fitted.

To study this effect, we simulated the motion of drifting electron with Garfield++ [29], under the proper electric and magnetic field conditions and the gas mixture used in the detector. For the magnetic field, we use the map based on previous measurements at DESY [30] and shown in Fig. 29.

From both data and simulation, we compute the inclination of tracks projected on the ERAM, and compare the results. Fig. 30 shows that the simulation is able to reproduce the vertical displacement of drifting electrons as observed in the data.

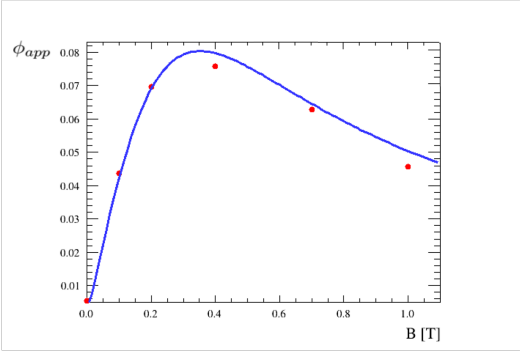

Figure 28: The red points show the observed track inclination on the magnetic field. In blue, the theoretical prediction of equation 10. The parameter δ is computed by the fit with result $\delta = 0.018$. Notice the slight deviation for high magnetic field, where the bending effect of the longitudinal magnetic field starts to be relevant.

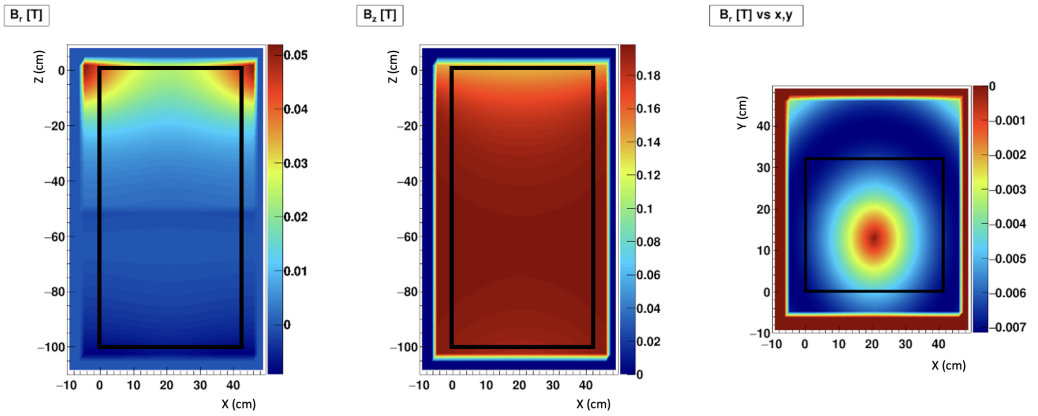

Figure 29: Map of the magnetic field. Left: radial component, top view. Central: longitudinal component, top view. Right: radial component, front view. The black boxes represent the contours of the TPC's drift volume. Notice the non negligible radial component of the field especially in the rear of the TPC.

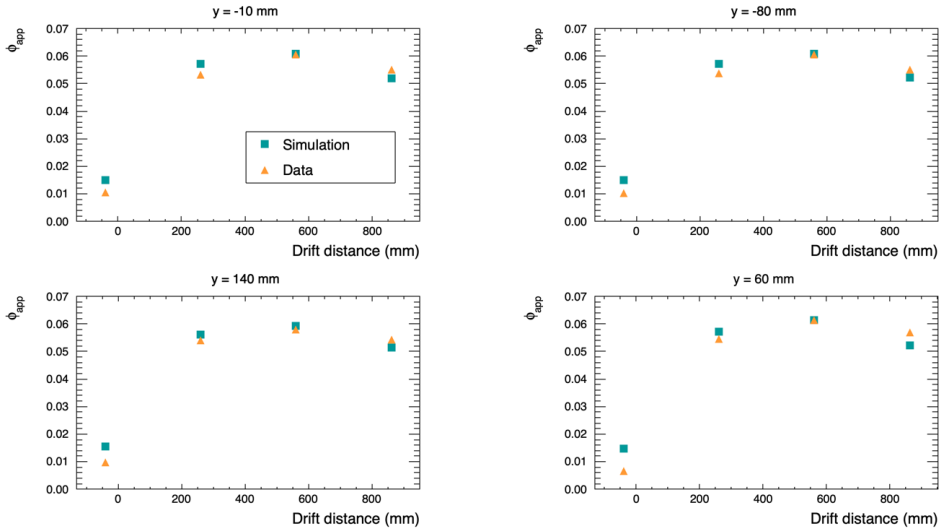

Figure 30: Vertical displacement of drifting electrons in data and simulations for B = 0.2 T. Each plot represents a different vertical position of the initial ionization track.

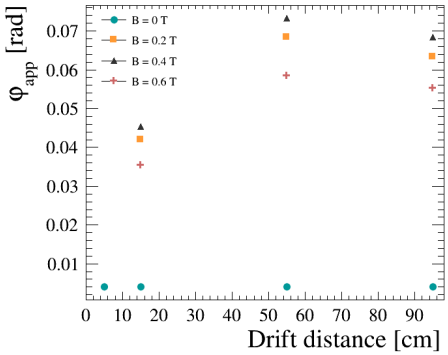

Figure 31: Vertical displacement of the tracks with respect to the drift distance for the beam parallel to the pad side for different values of magnetic field at the drift velocity of 78.7 mm/μs and peaking time of 200 ns.

The E×B effect dependence on magnetic field is shown in Fig 31, by plotting the vertical displacement for horizontal electrons of 1 GeV/c between the begin and the end of the track for different values of magnetic field and different drift distance. As expected, without magnetic field, there is no displacement in Y. When the magnetic field is on, as expected, the larger displacement is observed for small values of magnetic field.

E×B could also be responsible for the biases observed in the spatial resolution described in Sect. 8. In Fig. 32 we show the biases in the spatial resolution for different values of the magnetic field and as a function of the drift distance. The biases are small for all the drift distances when the magnetic field is off. When the magnetic field is on we observe larger biases for short and long drift distances, similarly to the ones shown in Fig. 17. The larger biases are observed for values of magnetic field of 0.2 and 0.4 T where the E×B effects are largest.

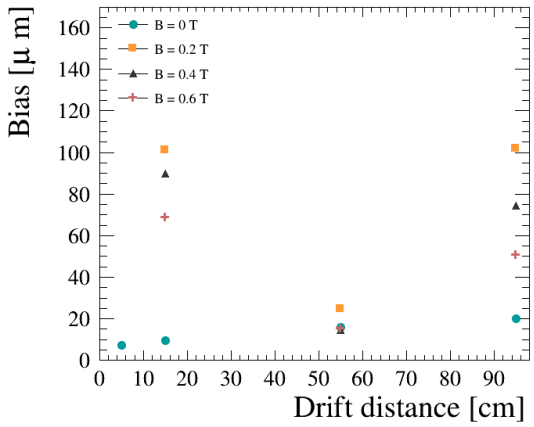

Figure 32: Track position bias with respect to the drift distance for the beam parallel to the pad side for different magnetic fields with drift velocity of 78.7 mm/μs and peaking times of 200 ns.

It should be noted that, as shown in previous sections, the impact of the E×B effect is not observed in the spatial resolution or in the dE/dx resolution and, for the purpose of this study, we did not try to account for this effect in the simulation where a perfect magnetic field is assumed.

12. Conclusions

In this paper we showed the performances of the prototype of the HA-TPCs for the T2K Near Detector upgrade during a test beam at DESY. The TPC was instrumented with one of the ERAM detectors that will be installed in the HA-TPCs and the HA-TPC electronics chain.

The test beam data allowed to characterize spatial and dE/dx resolution as a function of the angle of the track with respect to the ERAM plane for

all the drift distances of interest of T2K. Spatial resolution better than 800 µm is obtained for all the angles and all the drift distances using a dedicated clustering algorithm which is adapted to the track angle. Energy resolution better than 10% is obtained for all the angles.

The data are compared with a simulation of the ERAM response, including the features of the resistive layer. As shown in this paper, the simulation is able to satisfactory reproduce the observed charge sharing between neighboring pads. Spatial resolution and dE/dx resolution are also in good agreement between data and simulation.

Acknowledgements

The measurements leading to these results have been performed at the Test Beam Facility at DESY Hamburg (Germany), a member of the Helmholtz Association. The authors would like to thank the technical team at the DESY II accelerator and test beam facility for the smooth operation of the test beam and the support during the test beam campaign.
We acknowledge the support of CEA and CNRS/IN2P3, France; DFG, Germany; INFN, Italy; National Science Centre (NCN) and Ministry of Science and Higher Education (Grant No. DIR/WK/2017/05), Poland; MINECO and ERDF funds, Spain.
In addition, participation of individual researchers and institutions has been further supported by H2020 Grant No. RISE-GA822070-JENNIFER2 2020, MSCA-COFUND-2016 No.754496, ANR-19-CE31-0001, RFBR grants #19-32-90100, the Ministry of Science and Higher Education of Russia (contract #075-15-2020-778) the Spanish Ministerio de Economía y Competitividad (SEIDI - MINECO) under Grants No. PID2019-107564GB-I00 and SEV-2016-0588. IFAE is partially funded by the CERCA program of the Generalitat de Catalunya.

References

[1] K. Abe, et al., The T2K Experiment, Nucl. Instrum. Meth. A659 (2011) 106–135. arXiv:1106.1238, doi:10.1016/j.nima.2011.06.067.

[2] K. Abe, et al., Observation of Electron Neutrino Appearance in a Muon Neutrino Beam, Phys. Rev. Lett. 112 (2014) 061802. arXiv:1311.4750, doi:10.1103/PhysRevLett.112.061802.

[3] K. Abe, et al., Constraint on the matter–antimatter symmetry-violating phase in neutrino oscillations, Nature 580 (7803) (2020) 339–344, [Erratum: Nature 583, E16 (2020)]. arXiv:1910.03887, doi:10.1038/s41586-020-2177-0.

[4] K. Abe, et al., J-PARC Neutrino Beamline Upgrade Technical Design Report (8 2019). arXiv:1908.05141.

[5] K. Abe, et al., T2K ND280 Upgrade - Technical Design Report (1 2019). arXiv:1901.03750.

[6] P. A. Amaudruz, et al., The T2K Fine-Grained Detectors, Nucl. Instrum. Meth. A 696 (2012) 1–31. arXiv:1204.3666, doi:10.1016/j.nima.2012.08.020.

[7] N. Abgrall, et al., Time Projection Chambers for the T2K Near Detectors, Nucl. Instrum. Meth. A 637 (2011) 25–46. arXiv:1012.0865, doi:10.1016/j.nima.2011.02.036.

[8] I. Giomataris, R. De Oliveira, S. Andriamonje, S. Aune, G. Charpak, P. Colas, A. Giganon, P. Rebourgeard, P. Salin, Micromegas in a bulk, Nucl. Instrum. Meth. A560 (2006) 405–408. arXiv:physics/0501003, doi:10.1016/j.nima.2005.12.222.

[9] K. Abe, et al., Improved constraints on neutrino mixing from the T2K experiment with $\mathbf{3.13 \times 10^{21}}$ protons on target, Phys. Rev. D 103 (11) (2021) 112008. arXiv:2101.03779, doi:10.1103/PhysRevD.103.112008.

[10] K. Abe, et al., T2K ND280 Upgrade - Technical Design Report (2019). arXiv:1901.03750.

[11] S. Dolan, et al., Sensitivity of the upgraded T2K Near Detector to constrain neutrino and antineutrino interactions with no mesons in the final state by exploiting nucleon-lepton correlations, Phys. Rev. D 105 (3) (2022) 032010. arXiv:2108.11779, doi:10.1103/PhysRevD.105.032010.

[12] A. Blondel, et al., The SuperFGD Prototype Charged Particle Beam Tests, JINST 15 (12) (2020) P12003. arXiv:2008.08861, doi:10.1088/1748-0221/15/12/P12003.

[13] A. Korzenev, et al., A 4π time-of-flight detector for the ND280/T2K upgrade, JINST 17 (01) (2022) P01016. arXiv:2109.03078, doi:10.1088/1748-0221/17/01/P01016.

[14] D. Attie, Beam tests of Micromegas LC-TPC large prototype, JINST 6 (2011) C01007. doi:10.1088/1748-0221/6/01/C01007.

[15] D. Attié, et al., Performances of a resistive Micromegas module for the Time Projection Chambers of the T2K Near Detector upgrade, Nucl. Instrum. Meth. A 957 (2020) 163286. arXiv:1907.07060, doi:10.1016/j.nima.2019.163286.

[16] D. Attié, et al., Characterization of resistive Micromegas detectors for the upgrade of the T2K Near Detector Time Projection Chambers, Nucl. Instrum. Meth. A 1025 (2022) 166109. arXiv:2106.12634, doi:10.1016/j.nima.2021.166109.

[17] P. Baron, D. Calvet, E. Delagnes, X. de la Broise, A. Delbart, F. Druillole, E. Monmarthe, E. Mazzucato, F. Pierre, M. Zito, AFTER, an ASIC for the readout of the large T2K time projection chambers, IEEE Trans. Nucl. Sci. 55 (2008) 1744–1752. doi:10.1109/TNS.2008.924067.

[18] D. Calvet, Tdcm reference manual (2021).
URL https://indico.in2p3.fr/event/24090/contributions/94492/attachments/63769/87919/tdcm_reference_manual_V1-16.pdf

[19] R. Diener, et al., The DESY II Test Beam Facility, Nucl. Instrum. Meth. A 922 (2019) 265–286. arXiv:1807.09328, doi:10.1016/j.nima.2018.11.133.

[20] S. Agostinelli, et al., GEANT4–a simulation toolkit, Nucl. Instrum. Meth. A 506 (2003) 250–303. doi:10.1016/S0168-9002(03)01368-8.

[21] J. Apostolakis, S. Giani, L. Urban, M. Maire, A. V. Bagulya, V. M. Grichine, An implementation of ionisation energy loss in very thin absorbers for the geant4 simulation package, Nuclear Instruments and Methods in Physics Research Section A: Accelerators, Spectrometers, Detectors and Associated Equipment 453 (2000) 597–605. doi:10.1016/S0168-9002(00)00457-5.

[22] N. Abgrall, et al., Time Projection Chambers for the T2K Near Detectors, Nucl. Instrum. Meth. A637 (2011) 25–46. arXiv:1012.0865, doi:10.1016/j.nima.2011.02.036.

[23] M. S. Dixit, A. Rankin, Simulating the charge dispersion phenomena in micro pattern gas detectors with a resistive anode, Nucl. Instrum. Meth. A566 (2006) 281–285. arXiv:physics/0605121, doi:10.1016/j.nima.2006.06.050.

[24] M. Ester, H.-P. Kriegel, J. Sander, X. Xu, A density-based algorithm for discovering clusters in large spatial databases with noise, in: Proceedings of the Second International Conference on Knowledge Discovery and Data Mining, AAAI Press, 1996, pp. 226–231.

[25] R. Gluckstern, Uncertainties in track momentum and direction, due to multiple scattering and measurement errors, Nuclear Instruments and Methods 24 (1963) 381–389. doi:https://doi.org/10.1016/0029-554X(63)90347-1.
URL https://www.sciencedirect.com/science/article/pii/0029554X63903471

[26] K. Boudjemline, M. S. Dixit, J. P. Martin, K. Sachs, Spatial resolution of a GEM readout TPC using the charge dispersion signal, Nucl. Instrum. Meth. A574 (2007) 22–27. arXiv:physics/0610232, doi:10.1016/j.nima.2007.01.017.

[27] P. Colas, First test results from a Micromegas large TPC prototype, Nucl. Instrum. Meth. A623 (2010) 100–101. doi:10.1016/j.nima.2010.02.161.

[28] A. Bellerive, K. Boudjemline, R. Carnegie, M. Dixit, J. Miyamoto, E. Neuheimer, A. Rankin, E. Rollin, K. Sachs, J. P. Martin, V. Lepeltier, P. Colas, A. Giganon, I. Giomataris, Spatial resolution of a micromegas-tpc using the charge dispersion signal (2005). doi:10.48550/ARXIV.PHYSICS/0510085.
URL https://arxiv.org/abs/physics/0510085

[29] https://garfield.web.cern.ch/garfield.

[30] C. Grefe, Magnetic field map for a large tpc prototype (2008).